Shortwave and longwave radiative contributions to global warming under increasing CO_2

Aaron Donohoe[a,1], Kyle C. Armour[a], Angeline G. Pendergrass[b], and David S. Battisti[c]

[a]Department of Earth, Atmospheric and Planetary Sciences, Massachusetts Institute of Technology, Cambridge, MA 02139; [b]Advanced Study Program, National Center for Atmospheric Research, Boulder, CO 80307; and [c]Department of Atmospheric Sciences, University of Washington, Seattle, WA 98195

Edited by Robert E. Dickinson, The University of Texas at Austin, Austin, TX, and approved October 14, 2014 (received for review July 7, 2014)

In response to increasing concentrations of atmospheric CO_2, high-end general circulation models (GCMs) simulate an accumulation of energy at the top of the atmosphere not through a reduction in outgoing longwave radiation (OLR)—as one might expect from greenhouse gas forcing—but through an enhancement of net absorbed solar radiation (ASR). A simple linear radiative feedback framework is used to explain this counterintuitive behavior. It is found that the timescale over which OLR returns to its initial value after a CO_2 perturbation depends sensitively on the magnitude of shortwave (SW) feedbacks. If SW feedbacks are sufficiently positive, OLR recovers within merely several decades, and any subsequent global energy accumulation is because of enhanced ASR only. In the GCM mean, this OLR recovery timescale is only 20 y because of robust SW water vapor and surface albedo feedbacks. However, a large spread in the net SW feedback across models (because of clouds) produces a range of OLR responses; in those few models with a weak SW feedback, OLR takes centuries to recover, and energy accumulation is dominated by reduced OLR. Observational constraints of radiative feedbacks—from satellite radiation and surface temperature data—suggest an OLR recovery timescale of decades or less, consistent with the majority of GCMs. Altogether, these results suggest that, although greenhouse gas forcing predominantly acts to reduce OLR, the resulting global warming is likely caused by enhanced ASR.

global warming | climate feedbacks | energy accumulation

Global conservation of energy is a powerful constraint for understanding Earth's climate and its changes. Variations in atmospheric composition that result in a net positive energy imbalance at the top of atmosphere (TOA) drive global warming, with the world ocean as the primary reservoir for energy accumulation (1). In turn, increasing global surface temperature enhances emission of longwave (LW) radiation to space (the Planck response). A schematic of the global energy budget response to a step change in greenhouse gas (GHG) concentrations is illustrated in Fig. 1*A*: outgoing LW radiation (OLR) initially decreases because of enhanced LW absorption by higher GHG levels; as energy accumulates in the climate system, global temperature rises and OLR increases until the TOA energy balance is restored—when OLR once again balances the net absorbed solar radiation (ASR). In this canonical view of global warming, the net energy accumulation (shaded green area in Fig. 1*A*) is a consequence of decreased OLR driven by GHG forcing. In contrast, consider a hypothetical step change in solar insolation (Fig. 1*B*): ASR is increased, and energy accumulates until the climate warms sufficiently that OLR balances the ASR perturbation. In this case, the net energy accumulation (shaded red area in Fig. 1) is a consequence of increased ASR and opposed by the increased OLR (hatched green area in Fig. 1).

Is the present global warming caused by reduced OLR (as in Fig. 1*A*) or enhanced ASR (as in Fig. 1*B*)? Anthropogenic radiative forcing is dominated by LW active constituents, such as CO_2 and methane, and shortwave (SW) forcing agents, such as sulfate aerosols, are thought to be acting to reduce ASR compared with their preindustrial levels (2). Reduced OLR, thus, seems the likely cause of the observed global energy accumulation, although the limited length of satellite TOA radiation measurements precludes determination of the relative contributions of ASR and OLR by direct observation. Trenberth and Fasullo (3) considered global energy accumulation within the ensemble of coupled general circulation models (GCMs) participating in phase 3 of the Coupled Model Intercomparison Project (4) (CMIP3). They report that, under the Special Report on Emission Scenarios A1B emissions scenario, wherein increasing radiative forcing is driven principally by increasing GHG concentrations, OLR changes little over the 21st century and global energy accumulation is caused nearly entirely by enhanced ASR—seemingly at odds with the canonical view of global warming by reduced LW emission to space (outlined in Fig. 1*A*).

Here, we seek insight into this surprising result. In particular, we examine CO_2-only forcing scenarios as simulated by the CMIP5 ensemble of state of the art GCMs (5). Perturbing CO_2 alone permits a clean partitioning of radiative forcing and radiative response into their respective SW and LW components and allows an investigation into the relative contributions of reduced OLR and enhanced ASR to global energy accumulation. The CMIP5 multi-GCM mean response to a compounding 1% per year CO_2 increase (hereafter, 1% CO_2) is shown in Fig. 1*D*. Although CO_2 radiative forcing increases approximately linearly in time for 140 y (dotted lines in Fig. 1*D*), OLR changes little from its preindustrial value, and global energy accumulation is accomplished nearly entirely by increased ASR, consistent with the multi-GCM mean results in the work Trenberth and Fasullo (3). Perhaps even more striking is the response to an abrupt quadrupling of CO_2 (hereafter, 4× CO_2), which is shown in Fig. 1*C*: OLR initially decreases, like in Fig. 1*A*, but recovers to its unperturbed (preindustrial) value within only two decades;

EARTH, ATMOSPHERIC, AND PLANETARY SCIENCES

Significance

The greenhouse effect is well-established. Increased concentrations of greenhouse gases, such as CO_2, reduce the amount of outgoing longwave radiation (OLR) to space; thus, energy accumulates in the climate system, and the planet warms. However, climate models forced with CO_2 reveal that global energy accumulation is, instead, primarily caused by an increase in absorbed solar radiation (ASR). This study resolves this apparent paradox. The solution is in the climate feedbacks that increase ASR with warming—the moistening of the atmosphere and the reduction of snow and sea ice cover. Observations and model simulations suggest that even though global warming is set into motion by greenhouse gases that reduce OLR, it is ultimately sustained by the climate feedbacks that enhance ASR.

Author contributions: A.D. designed research; A.D., K.C.A., and A.G.P. performed research; A.D., K.C.A., and A.G.P. analyzed data; and A.D., K.C.A., A.G.P., and D.S.B. wrote the paper.

The authors declare no conflict of interest.

This article is a PNAS Direct Submission.

[1]To whom correspondence should be addressed. Email: thedhoe@mit.edu.

This article contains supporting information online at www.pnas.org/lookup/suppl/doi:10.1073/pnas.1412190111/-/DCSupplemental.

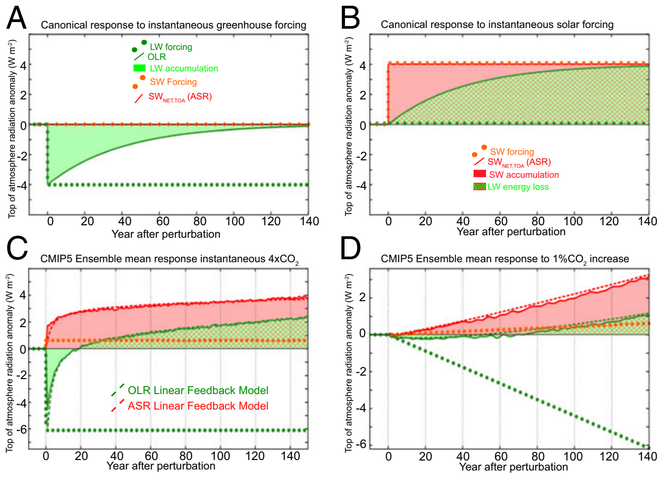

Fig. 1. (*A*) Idealized response of global mean radiation at the TOA to an instantaneous GHG forcing (green dots) assuming no SW feedback and a radiative adjustment e-folding time of 20 y. The green line shows the OLR response (anomaly from preindustrial), and the shaded green area shows the LW energy accumulation. (*B*) The same as in *A* but in response to an instantaneous SW forcing (red dots), with the red line showing the ASR response. In this case, the net energy accumulation is the difference between the SW energy accumulation (the shaded red area) and the LW increase (the hatched green area, where the hatching indicates that the LW response leads to a cooling of the climate system). (*C*) The ensemble average radiative response in the CMIP5 4× CO_2 simulations. The shaded area represents the energy accumulation by SW (red) and LW (green) anomalies, and the hatched area indicates energy loss by enhanced OLR. The dashed red and green lines show the predicted ensemble average ASR and OLR responses from the linear feedback model (Eqs. **1** and **2**). (*D*) The same as in *C* but for the CMIP5 ensemble average radiative response in the 1% CO_2 increase per year simulations (with linear increase in forcing as shown by dotted lines).

beyond this initial adjustment period, energy is lost due to enhanced OLR and gained solely by enhanced ASR.

Here, we propose a simple physical mechanism for this behavior. We show that the simulated global mean OLR and ASR responses (Fig. 1 *C* and *D*) and the short recovery time for OLR in particular can be understood in terms of a linear radiative feedback analysis. Moreover, the diversity of feedbacks across the CMIP5 GCMs explains the range in behavior across the models: in a majority of models, OLR recovers within several decades, and the subsequent global energy accumulation is caused by enhanced ASR; in a minority of models, OLR remains diminished for centuries, and global energy accumulation is driven by reduced OLR. Finally, we show that recent satellite observations constrain radiative feedbacks to be within the regime of relatively fast (approximately decades) OLR recovery under GHG forcing, similar to the majority of CMIP5 GCMs. Altogether, these results suggest that, although GHG forcing acts primarily in the LW, the resulting global warming is fundamentally a consequence of enhanced SW energy accumulation.

SW and LW Contributions to Energy Accumulation

We first consider in more detail the global radiative response of the CMIP5 GCMs to an abrupt GHG forcing (4× CO_2) (shown in Fig. 2). The evolution of OLR anomalies differs remarkably between GCMs (Fig. 2*D*). We characterize this range of responses by the time (τ_{cross}) that it takes for OLR to return to its unperturbed value*; τ_{cross} ranges from 2 to 231 y, with an ensemble mean of 19 y (see Fig. 4*A*).

To interpret these findings, we employ a commonly used linearization of the global TOA energy budget:

$$\frac{d(CT_S)}{dt} = F_{SW} + F_{LW} + (\lambda_{SW} + \lambda_{LW})T_S, \quad [1]$$

where T_S is the global mean surface temperature anomaly, and C is the time-dependent global heat capacity. Eq. **1** relates the rate of global heat content change to the rate of global TOA energy accumulation, which is given by the sum of SW and LW radiative forcings (F_{SW} and F_{LW}) and radiative responses ($\lambda_{SW} T_S$ and $\lambda_{LW} T_S$) (6). Anomalies in OLR and ASR can further be expressed as

$$ASR = F_{SW} + \lambda_{SW} T_S$$

and

$$-OLR = F_{LW} + \lambda_{LW} T_S. \quad [2]$$

The radiative feedbacks (λ_{SW} and λ_{LW}) can be estimated for each GCM by linear regression of ASR and OLR (Fig. 2 *C* and *D*) with T_S (Fig. 2*A*) over the period after 4× CO_2, wherein radiative forcing is approximately constant (7, 8). Moreover, the LW and SW components of CO_2 forcing (F_{LW} and F_{SW}) can be estimated by the $T_S = 0$ intercept of the regression.† Forcing and feedback values for the CMIP5 GCMs (Table S1) are consistent with those estimated by Andrews et al. (10).

As defined by Eq. **1**, the effective heat capacity C (Fig. 2*B*) is the time-integrated TOA energy accumulation divided by T_S. It has long been recognized that there is no single heat capacity (or characteristic relaxation time) of the climate system (11). Indeed, C increases with time as heat penetrates below the surface mixed layer and into the ocean interior (12–15). For the CMIP5 GCMs, C corresponds to an equivalent ocean depth of 50 m in the first decade after 4× CO_2 and increases over time, reaching an equivalent depth of several hundred meters after a century (Fig. 2*B*). The time evolution of C together with values of SW and LW feedbacks and forcing permit an iteration of Eq. **1** that accurately reproduces the surface temperature response T_S of each GCM (Fig. 2*A*). ASR and OLR predicted by Eq. **2** are in excellent agreement with their respective responses following 4× CO_2 (Fig. 2 *C* and *D*) and account for the vast majority (99%) of the variance in τ_{cross} across the models. Thus, a simple representation of climate feedbacks (Eqs. **1** and **2**) is all that is needed to understand the response of ASR and OLR under GHG forcing.

Insight into the GCM behavior can be gained by considering the values of ASR and OLR required to reach TOA energy balance (equilibrium) with an imposed GHG forcing. If forcing and feedbacks acted only in the LW (as in Fig. 1*A*), the OLR anomaly would increase from a value of $-F_{LW} = 0$ after 4× CO_2 (Eq. **2**), and global energy accumulation would be driven entirely by reduced OLR. In the multi-GCM mean, however, there is a substantial positive SW feedback of $\lambda_{SW} = 0.6$ W m^{-2} K^{-1} in addition to the negative LW feedback of $\lambda_{LW} = -1.7$ W m^{-2} K^{-1} (Fig. 3*A*). As a result, ASR increases with warming, contributing to global energy accumulation. Moreover, the positive λ_{SW} amplifies the equilibrium temperature response by a gain factor‡ ($G_{\lambda_{SW}}$) of ~1.5 relative to a system with LW feedbacks only, where

$$G_{\lambda_{SW}} \equiv 1/(1 + \lambda_{SW}/\lambda_{LW}). \quad [3]$$

The multi-GCM mean OLR must, therefore, increase by $1.5F_{LW}$ after 4× CO_2 (from $-F_{LW}$ to $0.5F_{LW}$) to reach equilibrium

*Note that, if OLR remains below its unperturbed value for the entirety of the 150-y simulation, we estimate τ_{cross} by linear extrapolation over the final century of the simulations. In this case, τ_{cross} should be considered a metric for the GHG forcing ameliorated by the response, because it is possible that OLR may never return to its unperturbed value.

†Radiative forcing by this method includes both the direct radiative forcing by the GHG and the effect of any tropospheric adjustments that occur on timescales of days to weeks (9).

‡We note that this gain factor differs from the commonly used feedback gain defined as the amplification of the equilibrium temperature response by radiative feedbacks (e.g., water vapor and surface albedo) relative to the response with the Planck feedback only (16, 17).

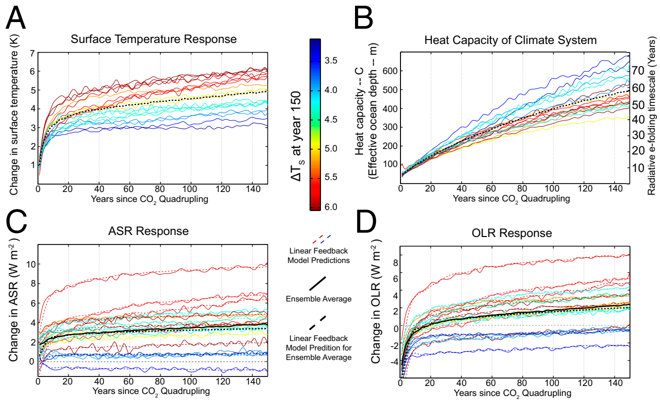

Fig. 2. (*A*) Time series of global mean surface temperature change in the CMIP5 4× CO_2 simulations. The individual models are indicated by the colored lines and color-coded by the temperature change at year 150 (the color bar is provided in the middle of the figure). The ensemble average is shown by the dashed black line. (*B*) The heat capacity of the climate system defined as the global time-integrated energy accumulation divided by surface temperature (Eq. **1**) given in units of the effective depth of a column of ocean (left axis) and units of radiative e-folding timescale (negative of heat capacity divided by the ensemble mean net radiative feedback $\lambda_{LW}+\lambda_{SW} = -1.1$ W m^{-2} K^{-1}; right axis). (*C*) Time series of the ASR response, where the solid lines are the GCM values and the dashed lines are the predictions of the linear feedback model (Eqs. **1** and **2**) using the GCM-specific heat capacity, forcings, and feedbacks. The solid black line is the ensemble mean of the GCM, and the dashed black line is the prediction of the linear feedback model using the ensemble average heat capacity, forcings, and feedbacks. (*D*) The same as in *C* except for the OLR response.

(Eq. **2**). Thus, OLR returns to its unperturbed value when $1F_{LW}/1.5F_{LW} \approx 66\%$ of the equilibrium temperature response has been realized. We estimate this timescale below. If we assume, for the moment, that the warming over the first several decades can be approximated with a constant heat capacity C, Eq. **1** can be readily solved for the time evolution of the surface temperature, giving

$$T_S = G_{\lambda_{SW}} \frac{F_{LW}}{\lambda_{LW}} \left(e^{\frac{-t}{\tau}} - 1\right), \qquad [4]$$

where

$$\tau = -\frac{C}{\lambda_{LW} + \lambda_{SW}}. \qquad [5]$$

From Eq. **4**, the ∼66% of the equilibrium temperature change required for OLR to recover to preindustrial values will be achieved at approximately time τ; that is, τ_{cross} is approximately equal to τ in the ensemble average. If we take the ensemble mean of C over the first century of the 4× CO_2 simulations as an upper bound on its value over the first several decades ($C \approx 250$ m from Fig. 2*B*), then Eq. **5** provides an upper bound on τ. For ensemble mean feedback values (Table S1), Eq. **5** gives $\tau \approx 29$ y, which is in good agreement with the CMIP5 ensemble mean OLR recovery timescale $\tau_{cross} = 19$ y. For all times after τ_{cross}, energy is lost through enhanced LW emission, and energy accumulation is solely due to enhanced ASR. Thus, the relative contributions of SW and LW anomalies to the total energy accumulation depend directly on the time that it takes for OLR to return to and cross its unperturbed value (τ_{cross}). In the multi-GCM mean, OLR takes only two decades to recover, and thus, energy accumulation is due primarily to enhanced ASR.

What, then, sets the large range of τ_{cross} across the CMIP5 GCMs? While a substantial fraction of equilibrium warming is achieved within the first several decades in all GCMs (15, 18)—due to the fast response of the surface components of the climate system (12)—the ASR and OLR responses to warming (and τ_{cross}) depend on the SW and LW feedbacks, which vary substantially (Fig. 3*A*). The dependence of τ_{cross} on the feedback parameters can be seen explicitly by solving the linear feedback model for τ_{cross} (under the assumption that $F_{SW} = 0$). Substituting Eq. **4** into Eq. **2** and identifying $t = \tau_{cross}$ as the time when OLR = 0 gives $F_{LW} = F_{LW} G_{\lambda_{SW}} (e^{\tau_{cross}/\tau} - 1)$, which has the solution

$$\tau_{cross} = -\tau \ln\left(1 - \frac{1}{G_{\lambda_{SW}}}\right). \qquad [6]$$

Eq. **6** reveals that the OLR recovery time is proportional to (*i*) the radiative e-folding timescale τ, which is on the order of several decades, and (*ii*) a factor $\ln(1 - 1/G_{\lambda_{SW}}) = \ln(-\lambda_{SW}/\lambda_{LW})$, which is ≈1 in the multi-GCM mean but varies by two orders of magnitude across the GCMs. A positive SW feedback amplifies warming, and thus enhances the OLR response and decreases the timescale for OLR recovery. Moreover, τ_{cross} is far more sensitive to changes in λ_{SW} than λ_{LW} over the parameter space realized in the GCMs (curves in Fig. 3*A*), suggesting that the intermodel differences in τ_{cross} are primarily controlled by variations in SW feedbacks. This result arises from a fundamental asymmetry in the dependence of OLR on λ_{SW} and λ_{LW}: a more positive λ_{SW} acts to amplify warming, which enhances OLR and decreases τ_{cross}; a less negative λ_{LW} similarly acts to amplify warming, which enhances OLR, but it also diminishes the OLR response per degree T_S change (Eq. **2**), altogether driving only small changes in τ_{cross}.

Despite its many simplifications, Eq. **6** provides a reasonable estimate of τ_{cross} as simulated by the GCMs, explaining 66% of the variance across models (Fig. 3*A*). In particular, it broadly captures the short OLR recovery time in the CMIP5 models with large and positive λ_{SW} values and the long OLR recovery time in models with a near-zero λ_{SW}. There are a few notable exceptions, however, where Eq. **6** predicts a substantially smaller τ_{cross} than is realized. τ_{cross} is underestmated in these models because we have not yet accounted for the SW component of CO_2 forcing, which is substantial in a few GCMs because of the rapid cloud adjustments that occur on timescales faster than surface temperature changes. Analogous to the SW feedback case discussed above, SW forcing amplifies the equilibrium temperature response by an SW forcing gain factor, $G_{F_{SW}}$, relative to the system with LW forcing only:

$$G_{F_{SW}} \equiv 1 + \frac{F_{SW}}{F_{LW}}. \qquad [7]$$

A positive SW forcing amplifies warming, enhancing the OLR response and decreasing τ_{cross}, whereas a negative SW forcing reduces warming, diminishing the OLR response and increasing τ_{cross}. Including the effects of SW feedbacks and forcing together gives a simple extension of Eq. **6**, wherein the gains are multiplicative (*SI Text*):

$$\tau_{cross} = -\tau \ln\left(1 - \frac{1}{G_{\lambda_{SW}}\, G_{F_{SW}}}\right). \qquad [8]$$

In the multi-GCM mean, F_{SW} is relatively small (Table S1), giving $G_{F_{SW}} \approx 1.1$ and modifying τ_{cross} little from that predicted by Eq. **6**. However, in some models, F_{SW} is a substantial fraction of the total CO_2 forcing (Fig. 3*B*), and thus, it has a large impact on τ_{cross}. With F_{SW} taken into account, Eq. **8** provides an excellent estimate of τ_{cross} as simulated by the GCMs, explaining 78% of the variance across models.

If a constant value $\tau \approx 29$ y is used in Eq. **8**, the dependence of τ_{cross} on the feedback and forcing gains can be visualized (curves in Fig. 3*B*). τ_{cross} has very steep gradients in the region where the product of $G_{\lambda_{SW}}$ and $G_{F_{SW}}$ approaches one, leading to a bimodal distribution of τ_{cross}, with OLR returning to unperturbed values either over a couple decades or at timescales longer than a century.

Although $G_{\lambda_{SW}}$ and $G_{F_{SW}}$ contribute equally to τ_{cross}, $G_{\lambda_{SW}}$ varies by a greater amount than $G_{F_{SW}}$ across the GCMs. Thus, it is SW feedback that most strongly controls the range of τ_{cross} and the relative contributions of OLR and ASR to global energy accumulation. However, in models with a sufficiently negative F_{SW} ($G_{F_{SW}} < 0$), τ_{cross} can be on the order of centuries, even with a large and positive λ_{SW} ($G_{\lambda_{SW}} > 0$). In general, OLR recovers on timescales of centuries in models with either weak SW feedbacks or weak (or negative) SW forcing, and OLR recovers on timescales of several decades in models with moderate SW feedbacks and SW forcing. This result can be further seen by varying only λ_{SW} and F_{SW} in the linear feedback model (Eq. **1**) and setting λ_{LW}, F_{LW}, and C equal to their ensemble mean values. The predicted values of τ_{cross} are in excellent agreement ($R^2 = 0.98$) with those simulated by the GCMs (Fig. 4*A*), except for two models with C much larger than the ensemble mean value. Importantly, allowing only λ_{SW} and F_{SW} to vary between models is sufficient to capture the clear separation between (*i*) those models with τ_{cross} on the order of centuries (black circles in Fig. 4*A*), where global energy accumulation is dominated by reduced OLR, and (*ii*) those models with τ_{cross} on the order of decades (colored circles in Fig. 4*A*), where global energy accumulation is dominated by enhanced ASR and opposed by enhanced OLR.

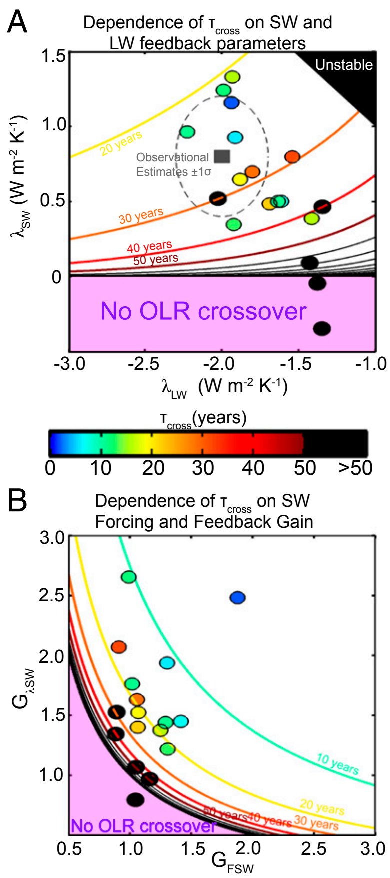

Fig. 3. (*A*) Contours show the sensitivity of τ_{cross} to LW and SW feedback parameters (λ_{LW} and λ_{SW}) in the linear feedback model (Eq. **6**) assuming the forcing is all in the LW and using a time-invariant heat capacity of 250-m ocean depth equivalent—the GCM mean over the first century. The shaded black region is the parameter space over which no equilibrium solution exists, and the shaded pink region is the parameter space over which the OLR never returns to its unperturbed value. The individual GCM results are given by the circles, which are color-coded by τ_{cross} (the color bar is provided in the middle of the figure). The gray ellipse and the dashed lines represent the observational estimates of λ_{LW} and $\lambda_{SW} \pm 1$ SD (σ). (*B*) The sensitivity of τ_{cross} to the SW forcing gain ($G_{F_{SW}}$) and SW feedback gain ($G_{\lambda_{SW}}$) assuming $\tau \sim 29$ y (the GCM mean over the first century) in Eq. **8**.

With these insights in mind, we return to the relative roles of ASR and OLR in driving global energy accumulation under the 1% CO_2 increase per year scenario, where GHG concentrations increase slowly over time, as in nature, rather than abruptly quadrupling. To quantify the relative roles of enhanced ASR and reduced OLR in transient energy accumulation, we define the SW energy accumulation ratio (SWEAR) to be the ratio of time-integrated energy accumulation via enhanced ASR to the time-integrated net radiative imbalance ($ASR - OLR$) over the 140 y of the 1% CO_2 simulations:

$$\mathrm{SWEAR} = \frac{\int ASR dt}{\int (ASR - OLR) dt}. \quad [9]$$

Values of SWEAR vary considerably across the GCMs (Fig. 4*B*), from near zero (energy accumulated primarily by reduced OLR) to near three (energy accumulated by enhanced ASR and lost by enhanced OLR). SWEAR between 0 and 1 indicates energy accumulation through both enhanced OLR and reduced OLR, whereas SWEAR above 0.5 indicates that ASR contributes more than one-half of global energy accumulation. In the multi-GCM mean, SWEAR is 1.1, indicating that OLR changes little and that net energy accumulation is accomplished entirely by enhanced ASR (Fig. 1*D*).

This range of GCM behavior under slowly increasing GHG forcing follows directly from the range of OLR recovery timescales τ_{cross} identified above under an abrupt change in GHGs, which, in turn, is set by intermodel differences in SW feedbacks and forcing. Indeed, the linear feedback model (Eqs. **1** and **2** with parameters estimated from 4× CO_2 as described above) iterated forward under 1% CO_2 captures the multi-GCM ASR and OLR response (dashed lines in Fig. 1*D*) and their variations across models. The linear feedback model, thus, also captures the inter-GCM variance in SWEAR (95%), where the vast majority (85%) of the inter-GCM variance can be explained by varying λ_{SW} and F_{SW} only (with λ_{LW}, F_{LW}, and C set to their ensemble means as above) (Fig. 4*B*).

Fig. 4*B* shows a clear separation between models with SWEAR ≤0.5 (OLR-dominated) and models with SWEAR ≥1 (ASR-dominated). Furthermore, models with SWEAR ≤0.5 are those with τ_{cross} on the order of centuries (Fig. 4*B*, black circles), and models with SWEAR ≥1 are the same as those with τ_{cross} on the order of decades (Fig. 4*B*, colored circles). This strong dependence of SWEAR on τ_{cross} can be understood by considering the response to 1% CO_2 as the superposition of many responses to an instantaneous CO_2 forcing, each initiated at a different time. More formally, the time (τ_{ramp}) at which OLR returns to its unperturbed value in response to a linear increase in CO_2 forcing can be approximated by (*SI Text*)

$$\tau_{ramp} = \frac{\tau}{1 - \frac{1}{G_{\lambda_{SW}} G_{F_{SW}}}} = \tau e^{\tau_{cross}/\tau}. \quad [10]$$

For models with τ_{cross} on the order of decades, τ_{RAMP} is also on the order of decades, and SWEAR is large. For models with τ_{cross} on the order of a century, τ_{RAMP} is on the order of several centuries, and SWEAR is small. Altogether, τ_{cross} explains 83% of the inter-GCM variance in SWEAR.

Observational Constraints on SW and LW Energy Accumulation

Global mean surface temperature has increased by about 0.85 K since the pre-industrial period (19) due to a global TOA energy accumulation driven by anthropogenic GHG emissions. Estimates

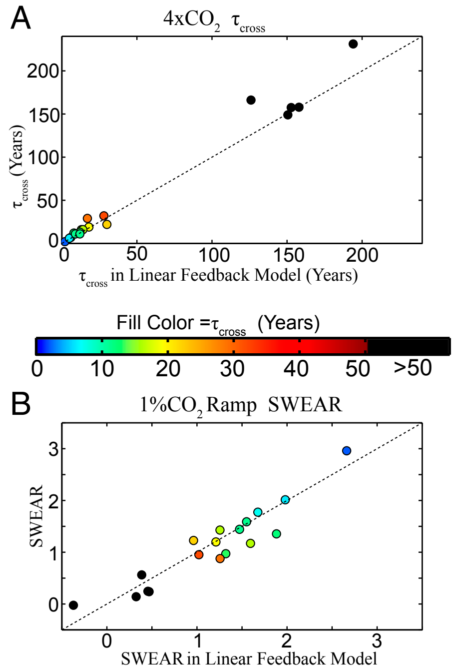

Fig. 4. (*A*) Scatterplot of τ_{cross} in the CMIP5 4× CO_2 simulations and those predicted by the linear feedback model (Eq. **8**) using the GCM-specific λ_{SW} and F_{SW} the GCM ensemble average λ_{LW}, F_{SW}, and heat capacity. The fill color of each circle indicates the τ_{cross} of each GCM in the 4× CO_2 simulation. The black dashed line is the 1:1 line. (*B*) The same as in *A* except for that scatterplot is of the SWEAR value in the 1% CO_2 increase per year simulations.

of the rate of global heat content change based on ocean temperature measurements indicate that the current TOA energy accumulation is on the order of 0.5–1 W m^{-2} (20, 21). Is the observed energy accumulation caused by reduced OLR or enhanced ASR? The limited accuracy and length of continuous satellite measurements of Earth's radiative budget (22–24) preclude direct determination of anomalies in OLR and ASR. However, the covariance of SW and LW radiation fluxes with global mean surface temperature over the satellite era permits an estimate of λ_{SW} and λ_{LW} (25). Moreover, given the arguments developed above, these feedback parameters can be used to estimate the relative contributions of ASR and OLR anomalies to the present day global energy accumulation.

Murphy et al. (25) estimated λ_{SW} and λ_{LW} using 6 y of data (2000–2005) from the Clouds and the Earth's Radiant Energy System Energy Balance Filled Project (24). Here, we extend these calculations with the now 14 y (2000–2013) of continuous satellite data and further account for changes in the global radiative forcing of stratospheric aerosols (26) and GHGs (27) over this period[§] (details in *SI Text*); λ_{SW} and λ_{LW} are calculated from the linear regression of monthly anomalies in forcing-adjusted ASR and OLR on monthly surface temperature anomalies (Fig. S2) from three different datasets: (*i*) the National Centers for Environment Prediction reanalysis surface air temperature (31), (*ii*) the Goddard Institute for Space Studies Surface Temperature Analysis (32), and (*iii*) the adaptation by Cowtan and Way (33) of the Climactic Research Unit of the United Kingdom Met Office's Hadley Center (34) surface temperature (version 4). The average of all calculations gives $\lambda_{SW} = 0.8 \pm 0.4$ and $\lambda_{LW} = -2.0 \pm 0.3$ W m^{-2} K^{-1}, where uncertainties represent 1 SD (additional details in *SI Text*). These feedback values are in good agreement with those simulated by the CMIP5 models, although λ_{SW} is at the upper end of the GCM range (Fig. 3*A*).

We can further estimate the effective global heat capacity C from observations by regressing global heat content anomalies [from ocean temperature measurements (35)] onto global mean surface temperature anomalies over the period 1970–2013 (Fig. S3), of which reliable ocean observations exist (20). This calculation gives an average value of $C = 90 \pm 30$ m of equivalent ocean depth, consistent with previous estimates (ref. 36 and references therein) and values over the first few decades of the CMIP5 simulations (Fig. 2*B*). Together, these observational estimates of the feedbacks and heat capacity can be used to estimate the Earth's natural timescale for radiative damping (τ) and OLR recovery (τ_{cross}) after a CO_2 increase: from Eqs. **5** and **6**, $\tau \approx 9$ y and $\tau_{cross} \approx 10$ y, respectively, consistent with but at the low end of the CMIP5 models because of an SW feedback that is at the high end of the model range. Despite the uncertainties in λ_{SW} and λ_{LW}, observations constrain the OLR recovery timescale to be on the order of decades (Fig. 3*A*), and thus, global warming in response to CO_2 forcing is expected to be a consequence of enhanced ASR.

We note that the above analysis assumes that CO_2 forcing acts predominantly in the LW. Although there are currently no direct observations of the SW component of CO_2 forcing induced by rapid cloud adjustments, Eq. **8** suggests that this SW forcing component would have to cancel a substantial fraction (>40%) of the LW component of CO_2 forcing before τ_{cross} becomes greater than several decades. If we use the CMIP5 GCMs as a guide to the range of possibilities, the SW component of CO_2 forcing cancels at most about 20% of the LW component and is more likely to substantially add to the total forcing (Fig. 3*B*), which would further reduce the timescale for OLR recovery and contribute to energy accumulation by enhanced ASR.

The short timescale τ_{cross} suggests that, if anthropogenic radiative forcing had acted predominantly in the LW and increased somewhat linearly over the last century, OLR would have recovered within a decade or so (Eq. **10**), beyond which time global energy accumulation would continue because of enhanced ASR. However, given a present GHG forcing of about 2.8 W m^{-2} (37), the increase in global surface temperature of about 0.85 K above preindustrial temperatures, and the observational estimate of λ_{LW}, Eq. **2** suggests an anomalous OLR of ≈ -0.8 W m^{-2}, implying that OLR is still contributing to global energy accumulation. This apparent discrepancy can be attributed to the effects of tropospheric aerosols, which are acting to reduce global warming (and thus, OLR) through a negative SW radiative forcing on the order of 1 W m^{-2} (although with large uncertainty) (37). Eq. **2** and our observational estimate of λ_{SW} then suggest an anomalous ASR of ≈ -0.2 W m^{-2} in the current climate. Altogether, these estimates imply that the current global energy accumulation is still dominated by decreased OLR. However, they also suggest that a transition to a regime of global energy accumulation dominated by enhanced ASR could occur with only 0.5 K global warming above present—by the middle of the 21st century if warming trends continue as projected.

Discussion and Conclusions

We have shown that, in most climate models, the OLR reduction associated with GHG forcing is alleviated within only a few decades and that the subsequent energy accumulation (and thus, global warming) is caused entirely by enhanced ASR. However, in some models, the OLR response is much slower. The range of model behaviors is readily understood in terms of a simple, linear feedback framework: positive SW feedbacks demand that ASR increases with warming and that OLR must ultimately become greater than its unperturbed value to achieve global energy balance with an imposed radiative forcing. The OLR recovery timescale is typically on the order of decades due to the fast response timescale of the surface components of the climate system and the negative LW feedbacks that strongly increase OLR with warming. Observational constraints also suggest an OLR recovery timescale on the order of decades. However, the current

[§]We do not account for changes in the radiative forcing of tropospheric aerosols since they have not changed substantially over this time (28–30).

global energy imbalance seems to be dominated by reduced OLR because of the substantial SW forcing associated with anthropogenic tropospheric aerosols, which have directly reduced ASR and indirectly reduced OLR by curtailing global warming.

The feedback analysis used here ignores time dependence (38) and other nonlinearities in climate feedbacks (39). Although both may be important for the details of the response, our results show that the OLR recovery timescale and the relative contributions of ASR and OLR to energy accumulation are largely governed by linear feedbacks (Fig. 4). At times, we simplified the analysis by assuming a constant effective global heat capacity (C) and associated single timescale of temperature response to forcing (τ). Although C increases over time (Fig. 2*B*) and there are, of course, multiple timescales of climate response (12, 15), accounting for these details (e.g., by representing a deep ocean heat capacity) makes no substantive changes to our results and conclusions. Indeed, surface temperature increases quickly after a CO_2 perturbation—much of the equilibrium temperature response is realized within the first few decades in all of the GCMs (Fig. 2*A*)—and the timescale of OLR recovery is most sensitive to the relative magnitudes of λ_{SW} and λ_{LW}. Moreover, when using a constant C, we have chosen a value that leads to a slight overestimate (underestimate) of τ_{cross} when τ_{cross} is small (large), providing an overall conservative estimate of τ_{cross} (Fig. 4*A*).

Although the differences in λ_{SW} across the CMIP5 models are primarily caused by differences in SW cloud feedbacks (40), the ensemble average value $\lambda_{SW} = 0.6$ W m^{-2} can be attributed to two robust and well-understood consequences of a warmer world: (*i*) the enhanced SW absorptivity of a moistened atmosphere (41) and (*ii*) the enhanced SW reflection associated with less-extensive snow and sea ice cover. SW absorption in the atmosphere leads to enhanced ASR by reducing the downwelling radiation incident on the top of clouds and the surface (42). Using radiative kernels (43, 44) and the changes in specific humidity in the CMIP5 4× CO_2 forcing experiments, we calculate an SW water vapor feedback of $+0.3 \pm 0.1$ W m^{-2} K^{-1}. The SW surface albedo feedback has a value of $+0.3 \pm 0.1$ W m^{-2} K^{-1} (43, 45). Thus, the positive λ_{SW} of the CMIP5 ensemble average and the resulting energy accumulation by enhanced ASR under GHG forcing can be expected based only on the robust physics of the water vapor feedback and the surface albedo feedback in the absence of any changes in clouds. Only if the SW cloud feedback is large and negative could the λ_{SW} become small and the resulting energy accumulation be dominated by reduced OLR. Instead, observations constrain λ_{SW} to be at the upper end of the CMIP5 range, implying that OLR recovers quickly in response to GHG forcing and that global warming is driven by enhanced ASR.

ACKNOWLEDGMENTS. We thank two anonymous reviewers for insightful comments. We also thank I. Held for insightful comments and D. Bacchus for energetic inspiration. A.D. was supported by a National Oceanic and Atmospheric Administration Global Change Fellowship. K.C.A. was supported by a James S. McDonnell Foundation Postdoctoral Fellowship. A.G.P. was funded by National Science Foundation Grant AGS-0960497.

1. Levitus S, et al. (2001) Anthropogenic warming of Earth's climate system. *Science* 292(5515):267–270.
2. Collins W, et al. (2006) Radiative forcing by well-mixed greenhouse gases: Estimates from climate models in the intergovernmental panel on climate change (ipcc) fourth assessment report (ar4). *J Geophys Res* 111(D14):D14317.
3. Trenberth KE, Fasullo JT (2009) Global warming due to increasing absorbed solar radiation. *Geophys Res Lett* 36(7).
4. Meehl GA, et al. (2007) The WCRP CMIP3 multi-model dataset: A new era in climate change research. *Bull Am Meteorol Soc* 88(9):1383–1394.
5. Taylor K, Stouffer R, Meehl G (2012) An overview of cmip5 and the experiment design. *Bull Am Meteorol Soc* 93(4):485–498.
6. Budyko M (1969) The effect of solar radiation variations on the climate of the earth. *Tellus B Chem Phys Meteorol* 21(5):611–619.
7. Gregory JM, et al. (2004) A new method for diagnosing radiative forcing and climate sensitivity. *Geophys Res Lett* 31(3):L032051.
8. Gregory J, Webb M (2008) Tropospheric adjustment induces a cloud component in co_2 forcing. *J Clim* 21(1):58–71.
9. Cao L, Bala G, Caldeira K (2012) Climate response to changes in atmospheric carbon dioxide and solar irradiance on the timescale of days to weeks. *Environ Res Lett* 7(3):03415.
10. Andrews T, Gregory J, Webb M, Taylor K (2012) Forcing, feedbacks and climate sensitivity in cmip5 coupled atmosphere-ocean climate models. *Geophys Res Lett* 39(9):L09712.
11. Crowley TJ, North GR (1988) Abrupt climate change and extinction events in Earth history. *Science* 240(4855):996–1002.
12. Held I, et al. (2010) Probing the fast and slow components of global warming by returning abruptly to preindustrial forcing. *J Clim* 23(9):2418–2427.
13. Kim K, North G, Huang J (1992) On the transient response of a simple coupled climate system. *J Geophys Res* 97(D9):10069–10081.
14. Wigley T, Raper S (1987) The thermal expansion of sea water associated with global warming. *Nature* 330(6144):127–131.
15. Kostov Y, Armour KC, Marshall J (2014) Impact of the atlantic meridional overturning circulation on ocean heat storage and transient climate change. *Geophys Res Lett* 41(6):2108–2116.
16. Roe G (2009) Feedbacks, time scales, and seeing red. *Annu Rev Earth Planet Sci* 37:93–115.
17. Hansen J, Lacis A, Rind D, Russell G, Stone P (1984) Climate sensitivity: Analysis of feedback mechanisms. *Climate Processes and Climate Sensitivity*, eds Hansen JE, Takahashi T (American Geophysical Union, Washington).
18. Caldeira K, Myhrvold N (2013) Projections of the pace of warming following an abrupt increase in atmospheric carbon dioxide concentration. *Environ Res Lett* 8(3):34039–34040.
19. Hartmann D, et al. (2013) *Climate Change 2013: The Physical Science Basis. Contribution of Working Group I to the Fifth Assessment Report of the Intergovernmental Panel on Climate Change*, eds Stocker T, et al. (Cambridge Univ Press, Cambridge, UK), Chap 2.
20. Trenberth KE, Fasullo JT, Kiehl J (2009) Earth's global energy budget. *Bull Am Meteorol Soc* 90(3):311–324.
21. Loeb NG, et al. (2012) Observed changes in top-of-the-atmosphere radiation and upper-ocean heating consistent within uncertainty. *Nat Geosci* 5(2):110–113.
22. Barkstrom, et al. (1989) Earth radiation budget (erbe) archival and april 1985 results. *Bull Am Meteorol Soc* 70(10):1254–1262.
23. Wielicki B, et al. (1996) Clouds and the earth's radiant energy system (CERES): An earth observing system experiment. *Bull Am Meteorol Soc* 77(5):853–868.
24. Loeb NG, et al. (2009) Towards optimal closure of the earth's top-of-atmosphere radiation budget. *J Clim* 22(3):748–766.
25. Murphy DM, et al. (2009) An observationally based energy balance for the earth since 1950. *J Geophys Res* 114(D17):16.
26. Solomon S, et al. (2011) The persistently variable "background" stratospheric aerosol layer and global climate change. *Science* 333(6044):866–870.
27. Masarie MPT (1995) Extension and integration of atmospheric carbon dioxide data into a globally consistent measurement record. *J Geophys Res* 100(D6):11593–11610.
28. Murphy DM (2013) Little net clear-sky radiative forcing from recent regional redistribution of aerosols. *Nat Geosci* 6(4):258–262.
29. Carslaw KS, et al. (2013) Large contribution of natural aerosols to uncertainty in indirect forcing. *Nature* 503(7474):67–71.
30. Stevens B (2013) Aerosols: Uncertain then, irrelevant now. *Nature* 503(7474):47–48.
31. Kalnay E, et al. (1996) The NCEP/NCAR 40-year reanalysis project. *Bull Amer Meteor Soc* 77(3):437–471.
32. Hansen J, Ruedy R, Glascoe J, Sato M (1999) Giss analysis of surface temperature change. *J Geophys Res* 104(D24):30997–31022.
33. Cowtan K, Way R (2014) Coverage bias in the hadcrut4 temperature series and its impact on recent temperature trends. *Quart J R Meteor Soc* 140(683):1935–1944.
34. Morice CP, Kennedy J, Rayner N, Jones P (2012) Quantifying uncertainties in global and regional temperature change using an ensemble of observational estimates: The hadcrut4 dataset. *J Geophys Res* 117(D8):D08101.
35. Antonov J, et al. (1998) *World Ocean Atlas 1998 Vol. 1: Temperature of the Atlantic Ocean* (National Oceanographic Data Center, Boulder, CO).
36. Schwartz S (2007) Heat capacity, time constant, and sensitivity of earth's climate system. *J Geophys Res* 112(D24):D15103.
37. Myhre G, et al. (2013) Anthropogenic and Natural Radiative Forcing. *Climate Change 2013: The Physical Science Basis. Contribution of Working Group I to the Fifth Assessment Report of the Intergovernmental Panel on Climate Change*, eds Stocker T, et al. (Cambridge Univ Press, Cambridge, United Kingdom).
38. Armour K, Bitz C, Roe G (2013) Time-varying climate sensitivity from regional feedbacks. *J Clim* 26(13):4518–4534.
39. Feldl N, Roe G (2013) The nonlinear and nonlocal nature of climate feedbacks. *J Clim* 26:8289–8304.
40. Bony S, et al. (2006) How well do we understand climate change feedback processes? *J Clim* 19(21):3345–3482.
41. Donohoe A, Battisti D (2013) The seasonal cycle of atmospheric heating and temperature. *J Clim* 26(14):4962–4980.
42. Donohoe A, Battisti D (2011) Atmospheric and surface contributions to planetary albedo. *J Clim* 24(16):4401–4417.
43. Soden B, Held I (2006) An assessment of climate feedbacks in coupled ocean-atmosphere models. *J Clim* 19(14):3354–3360.
44. Previdi M (2010) Radiative feedbacks on global precipitation. *Environ Res Lett* 5(2):025211.
45. Collins R (2013) Surface albedo feedbacks from climate variability and change. *J Geophys Res* 118(7):2827–2834.

Supporting Information

Donohoe et al. 10.1073/pnas.1412190111

SI Text

Here, we derive the analytical solutions to the OLR recovery time in response to an instantaneous and linearly increasing GHG forcing (τ_{cross} in Eq. **6** and τ_{ramp} in Eq. **8**). We also elaborate on the observational calculations of the linear feedback parameters (λ_{SW} and λ_{LW}) and the climate system heat capacity (C).

Derivation of Eqs. 6 and 8. The time evolution of global mean surface temperature from the solution of Eq. **1** under an instantaneous greenhouse forcing and with a time-invariant C is

$$T_S = \frac{F_{LW}+F_{SW}}{\lambda_{LW}+\lambda_{SW}}\left(e^{\frac{-t}{\tau}}-1\right). \qquad \textbf{[S1]}$$

The time evolution of the OLR is found by substituting Eq. **S1** into Eq. **2**:

$$OLR(t) = -F_{LW} + \frac{(F_{LW}+F_{SW})\lambda_{LW}}{\lambda_{LW}+\lambda_{SW}}\left(1-e^{\frac{t}{\tau}}\right) \qquad \textbf{[S2a]}$$

$$= -F_{LW} + F_{LW}\left[\underbrace{\left(1+\frac{F_{SW}}{F_{LW}}\right)}_{G_{F_{SW}}}\underbrace{\left(\frac{1}{1+\frac{\lambda_{SW}}{\lambda_{LW}}}\right)}_{G_{\lambda_{SW}}}\right]\left(1-e^{\frac{t}{\tau}}\right). \qquad \textbf{[S2b]}$$

Identifying $OLR(t=\tau_{cross})=0$ in expression **S2b** and solving for τ_{cross} gives Eq. **6** in the text.

The ramped forcing in the 1% CO_2 runs can be thought of as the summation of many heaviside functions, each starting at a different time step, in the limit that the step size goes to zero. Therefore, the surface temperature response to a ramped forcing in the linear feedback model is equal to the sum of the responses to an instantaneous forcing (Eq. **S1**), each starting at a different time after the forcing has started:

$$T_{S,ramp} = \int_0^t \frac{dF}{dt}\,\frac{1-e^{\frac{-t}{\tau}}}{-(\lambda_{LW}+\lambda_{SW})}dt \qquad \textbf{[S3a]}$$

$$= \frac{\dot{F}}{-(\lambda_{LW}+\lambda_{SW})}\left(\underbrace{t-\tau}_{steady} + \underbrace{\tau e^{\frac{-t}{\tau}}}_{transient}\right) \qquad \textbf{[S3b]}$$

as shown by Kim et al. (1). $\dot{F}$ is the time derivative of the forcing, which is constant in this experiment. The first term in expression **S3b** represents the long-term response to the ramped forcing, in which the temperature increases linearly in time, and the second term represents the transient response, which decays on the same e-folding timescale found in the analysis of the 4× CO_2 runs. We note that the long-term temperature change is not equal to the time-integrated forcing divided by the feedback (which is the case for the equilibrium response to instantaneous forcing) but is offset from this solution by the equivalent of τ y of integrated forcing. In this case, the TOA energy balance is never achieved, but rather, the TOA energy imbalance becomes constant in time and drives a constant surface temperature tendency (surface temperature increases linearly in time), such that $\dot{F}$ is balanced by the surface temperature tendency times the sum of the feedback parameters. We note that, after several e-folding timescales (>50 y), the system nearly asymptotes to the steady linear increase.

The time evolution of the OLR can be found by substituting expression **S3b** into Eq. **2**:

$$OLR_{RAMP}(t) = -\dot{F}_{LW}t + \qquad \textbf{[S4a]}$$

$$\frac{\lambda_{LW}}{\lambda_{LW}+\lambda_{SW}}\left(\dot{F}_{LW}+\dot{F}_{SW}\right)\left(t-\tau+\tau e^{\frac{-t}{\tau}}\right) \qquad \textbf{[S4b]}$$

$$\approx \dot{F}_{LW}t\left(G_{F_{SW}}\;G_{\lambda_{SW}}\left(1-\frac{\tau}{t}\right)-1\right), \qquad \textbf{[S4c]}$$

where we have ignored the transient term in the approximation. Identifying $t=\tau_{ramp}$ when the left-hand side of expression **S4c** = 0 and solving for τ_{ramp} gives Eq. **10**.

Observational Estimates of λ_{SW} and λ_{LW}. The covariability of the global mean forcing adjusted ASR and OLR with the global average surface temperature is used to estimate λ_{SW} and λ_{LW}. Radiation data are from the Clouds and the Earth's Radiant Energy System Energy Balanced and Filled Product (2) and span the period 2000–2013. Monthly anomalies are used, because the seasonal cycle of reflected SWs is primarily because of the spatial distribution of insolation and planetary albedo (3) and thus, not a consequence of radiative feedbacks. Insolation variability (global mean 2σ = 0.2 W m^{-2}) is removed from the Clouds and the Earth's Radiant Energy System Energy Balanced and Filled Product data, because this solar variability leads to variations in TOA radiation that are externally forced and unrelated to climate feedbacks. The impact of insolation anomalies on the reflected SW radiation is also removed by subtracting the anomalous insolation times the climatological planetary albedo from the upwelling SW. This method is equivalent to calculating anomalies in planetary albedo and multiplying by the climatological insolation to convert to watts meter^{-2}.

We calculate the observed SW forcing caused by stratospheric aerosols and the observed LW forcing associated with increased GHGs as follows. The interannual variability of stratospheric aerosol forcing is calculated from the aerosol optical depth by Solomon et al. (4), who used combined satellite observations from the Stratospheric Aerosol and Gas Experiment II (1990–2005), Global Ozone Monitoring by Occulation of Stars (2002–2009), and the Cloud-Aerosol Lidar and Infrared Pathfinder Satellite Observations (2006–2010) to produce a continuous record of aerosol optical depth above 15 km between 50 S and 50 N. We convert the aerosol optical depth to TOA SW forcing using a conversion factor of 25 W m^{-2} (5). GHG forcing is calculated separately for CO_2, CH_4, and N_2O. Monthly, global mean CO_2 concentrations from the National Oceanic and Atmospheric Administration Earth System Research Laboratory (6) are converted to radiative forcing using

$$F_{LW_{CO_2}} = 5.57\text{ W m}^{-2}\ln\left(\frac{CO_2}{CO_{2,REF}}\right), \qquad \textbf{[S5]}$$

where $CO_{2,REF}$ is the reference concentration, taken here as the time average over the analysis period. CH_4 and N_2O forcings are taken from the National Oceanic and Atmospheric Administration

Annual Greenhouse Gas Index (http://esrl.noaa.gov/gmd/aggi/aggi.html). The annual mean radiative forcing data are linearly interpolated to monthly resolution. The GHG forcings are converted to anomalies over the observational period and subtracted from the global mean OLR anomalies before our analysis of the feedback factor λ_{LW}.

Three different sets of surface temperature data are considered here: (*i*) National Centers for Environment Prediction (NCEP) reanalysis surface air temperature (7), (*ii*) the Goddard Institute for Space Studies Surface Temperature Analysis (GISTEMP) (8), and (*iii*) the modification by Cowtan and Way (9) of the Met Office Hadley Centre surface temperature dataset (10) version 4 (HadCRUT4). All data are converted to anomalies from the climatological annual cycle over the period 2000–2013. Grid points with missing data at any time over the analysis period are excluded. We use globally (spatially weighted) averaged data in our analyses. In all three datasets, the global average temperature exhibits a significant (95% confidence interval) upward trend. The amplitudes of the trend—quantified by the regression coefficient times one-half of the 13-y analysis period—are 0.08, 0.02, and 0.07 K for the NCEP, GISTEMP, and Hadley Centre data, respectively. The amplitudes of the detrended, monthly, and globally averaged temperatures (2σ) are 0.28, 0.22, and 0.25 K, respectively, in the NCEP, GISTEMP, and Hadley Centre data. In all cases, the amplitude of variability in the detrended data exceeds the amplitude associated with the trend; the interannual variability of global average temperature exceeds the global warming signal associated with increasing GHGs over the 13-y analysis period. We note that we do not detrend the data before our analysis, because the signals that we wish to capture are the (forcing-adjusted) radiation changes as the planet warms (either because of global warming or internal variability).

The regression slope between global averaged OLR and global averaged surface temperature anomalies, which we equate with λ_{LW}, ranges from -2.2 ± 0.3 W m^{-2} K^{-1} (uncertainty is 1σ) with the GISTEMP data (Fig. S1*A*) to -1.7 ± 0.2 W m^{-2} K^{-1} with the NCEP reanalysis surface temperature data (Table S2). For all three temperature datasets, the net SW radiation at the TOA (forcing and insolation-adjusted) increases with global mean temperature, consistent with the positive SW feedback found previously (11). We find λ_{SW} to be $+0.8 \pm 0.4$, $+0.7 \pm 0.4$, and $+0.9 \pm 0.4$ W m^{-2} K^{-1} using the GISTEMP (Fig. S1*B*), NCEP reanalysis, and Hadley Centre temperature data, respectively. Averaging across all three analyses yields $\lambda_{SW} = +0.8 \pm 0.4$ W m^{-2} K^{-1} and $\lambda_{LW} = -2.0 \pm 0.4$ W m^{-2} K^{-1}. These values place the SW feedback within the range spanned by the CMIP5 models but are somewhat greater than the ensemble average λ_{SW} of +0.6 W m^{-2} K^{-1}. The observed LW feedback is slightly more stabilizing than the CMIP5 model's ensemble average λ_{LW} of −1.7 W m^{-2} K^{-1}.

For all three temperature datasets, correlation between temperature and each of the radiation components is significant at the 99% confidence interval, despite the small fraction of variance explained (r^2 averages 0.28 for OLR and 0.05 for ASR). The uncertainty in the feedback parameters (σ_λ) is estimated by way of the SD of each time series σ, the correlation coefficient between the time series r, and the degrees of freedom N^* using the approximation (12)

$$\sigma_{\lambda_{SW}} = \frac{\sigma_{ASR}\sqrt{1-r^2_{ASR,T_S}}}{\sigma_{T_S}\sqrt{N^*}}. \quad \textbf{[S6]}$$

A similar expression holds for the uncertainty in λ_{LW}, with ASR replaced by OLR. The degrees of freedom (N^*) are calculated from the lag 1-mo autocorrelation, $r(\Delta t)$, of T_S and OLR/ASR and the number of months in the record (N) (13):

$$N^* = N\frac{1-r(\Delta t)_{T_S}\, r(\Delta t)_{ASR}}{1+r(\Delta t)_{T_S}\, r(\Delta t)_{ASR}}. \quad \textbf{[S7]}$$

The 1-mo lag autocorrelation of T_S ($r(\Delta t)_{T_S}$) averaged over the three temperature datasets is 0.61. The 1-mo lag autocorrelations in ASR and OLR are significantly lower (0.10 and 0.31, respectively). As a result, the effective degrees of freedom in the 160-mo record used to calculate the regression of temperature with ASR are N^* = 143, whereas those for temperature with OLR are N^* = 113. Eq. **S6** lends insight into why the error bounds (σ_λ) on λ_{SW} and λ_{LW} are relatively small, despite the weak correlation between the TOA radiation and the surface temperature. In the limiting case of no physical relationship between ASR and T_S, one would expect a regression coefficient of zero with some variation because of random chance correlations within the sample realized. The maximum possible regression is equal to $\sigma_{ASR}/\sigma_{T_S} = 4$ W m^{-2} K^{-1}, which would be realized if the variables were perfectly correlated, in this hypothetical example by random chance. Random correlations are less likely with larger samples, and thus, the regression coefficient converges to its true value as the sample size increases. In our case, with order of 100 independent data, it is unlikely (1σ) to get a random correlation coefficient that exceeds 0.1 ($1/\sqrt{N^*}$) in magnitude. Therefore, the regression coefficient caused by random noise should not exceed (4 W m^{-2} K^{-1}/10 =) 0.4 W m^{-2} K^{-1}. Hence, the calculated λ_{SW} of 0.8 W m^{-2} K^{-1} is statistically significant. The feedback parameters are statistically significant, because it is highly unlikely to find values of this magnitude in the absence of a true feedback process, even if processes other than temperature feedbacks make a larger contribution to the TOA radiation variance. To further see this point, we randomly subsample the surface temperature and TOA radiation data and create 10,000 estimates of the feedback parameters using a (bootstrapped) Monte Carlo simulation. For each estimate, we create a time series of each dataset with 160 monthly values by randomly sampling the full dataset with replacement. The resulting probability distribution function for λ_{SW} and λ_{LW} agrees very well with that expected from Eq. **S6** (Fig. S1*C*). We emphasize that it is highly unlikely that $\lambda_{SW} < 0$; fewer than 1% of the Monte Carlo realizations give negative values for λ_{SW}.

Observational Estimate of Climate System Heat Capacity. Here, we estimate the heat capacity of the climate system from observations for the period 1970–2012. As defined by Eq. **1**, the heat capacity is the time-integrated global energy accumulation divided by the resulting global mean surface temperature change. The changes in the energy content of the atmospheric column, land surface, and cryosphere are negligible compared with the changes in energy content in the ocean. Hence, the time-integrated energy accumulation in the climate system is equal to the ocean heat content anomaly. The latter is provided by data from the World Ocean Atlas (14) (Fig. S2*A*). The regression coefficient between ocean heat content anomalies (relative to the 1970–2012 period) and global mean surface temperature anomalies from NCEP reanalysis, GISTEMP, and the Hadley Centre datasets give three estimates of the climate system heat capacity, C. These values range from 10 ± 2 to 14 ± 3 W m^{-2} y K^{-1} between the NCEP reanalysis and HadCRUT4 (Fig. S2*B*), with a central estimate of 12 ± 3 W m^{-2} y K^{-1} or 90 ± 30 m equivalent ocean depth. (An equivalent ocean depth is defined by the heat capacity of an ocean covering the entire surface area of the Earth.) We note that the maximum value of C determined from any specific 10-y period in all temperature datasets is 150-m equivalent ocean depth, which sets an upper bound on the radiative e-folding timescale (τ) of 15 y given our estimates of λ_{SW} and λ_{LW}.

1. Kim K, North G, Huang J (1992) On the transient response of a simple coupled climate system. *J Geophys Res* 97(D9):10069–10081.
2. Loeb NG, et al. (2009) Towards optimal closure of the earth's top-of-atmosphere radiation budget. *J Clim* 22(3):748–766.
3. Donohoe A, Battisti D (2011) Atmospheric and surface contributions to planetary albedo. *J Clim* 24(16):4401–4417.
4. Solomon S, et al. (2011) The persistently variable "background" stratospheric aerosol layer and global climate change. *Science* 333(6044):866–870.
5. Hansen J (1992) Efficacy of climate forcings. *J Geophys Res* 110(D18):D18104.
6. Masarie MPT (1995) Extension and integration of atmospheric carbon dioxide data into a globally consistent measurement record. *J Geophys Res* 100(D6):11593–11610.
7. Kalnay E, et al. (1996) The NCEP/NCAR 40-year reanalysis project. *Bull Amer Meteor Soc* 77(3):437–471.
8. Hansen J, Ruedy R, Glascoe J, Sato M (1999) Giss analysis of surface temperature change. *J Geophys Res* 104(D24):30997–31022.
9. Cowtan K, Way R (2014) Coverage bias in the hadcrut4 temperature series and its impact on recent temperature trends. *Quart J R Meteor Soc* 140(683):1935–1944.
10. Morice CP, Kennedy J, Rayner N, Jones P (2012) Quantifying uncertainties in global and regional temperature change using an ensemble of observational estimates: The hadcrut4 dataset. *J Geophys Res* 117(D8):D08101.
11. Murphy DM, et al. (2009) An observationally based energy balance for the earth since 1950. *J Geophys Res* 114(D17):16.
12. Sveshnikov A (1979) *Problems in Probability Theory, Mathematics Statistics and Theory of Random Functions* (Saunders, Philadelphia).
13. Hartmann D (2014) *Objective Analysis* (University of Washington Department of Atmospheric Sciences, Seattle).
14. Antonov J, et al. (1998) *World Ocean Atlas 1998 Vol. 1: Temperature of the Atlantic Ocean* (National Oceanographic Data Center, Boulder, CO).

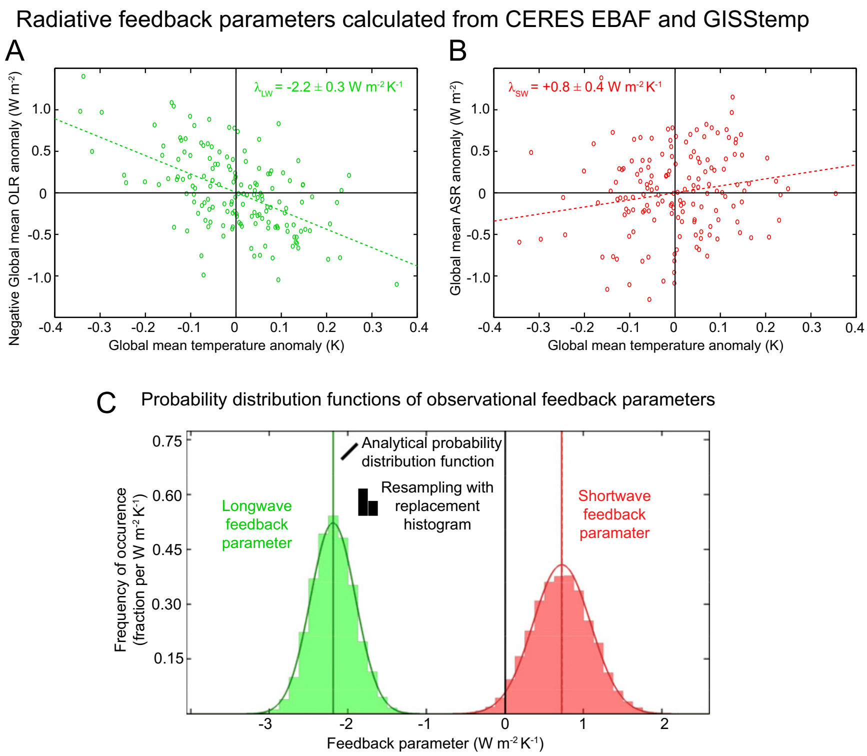

Fig. S1. (*A*) Scatterplot of the (forcing-adjusted) anomaly in net LW radiation at the TOA (negative OLR) from the Clouds and the Earth's Radiant Energy System Energy Balanced and Filled (CERES EBAF) Product and the global mean surface temperature anomaly from GISTEMP. The circles are monthly anomalies from climatology (2000–2013), and the dashed line is the linear best fit with slope equal to λ_{LW} (the value and the uncertainty are shown). (*B*) The same as in *A* except for ASR (ordinate) with the resulting estimate of λ_{SW}. (*C*) Histogram of observational feedback parameters calculated from a 10,000-member (bootstrapped) Monte Carlo resampling of the CERES EBAF radiation data and GISTEMP temperature data (shaded blocks). LW estimates are shown in green, and SW estimates are shown in red. The solid lines are the analytical probability distribution functions derived from the full record (Eqs. **S6** and **S7**). The mean of the Monte Carlo estimate is shown by the dashed vertical line, and the regression coefficient derived from the full record is shown by the solid vertical line (the lines are on top of one another).

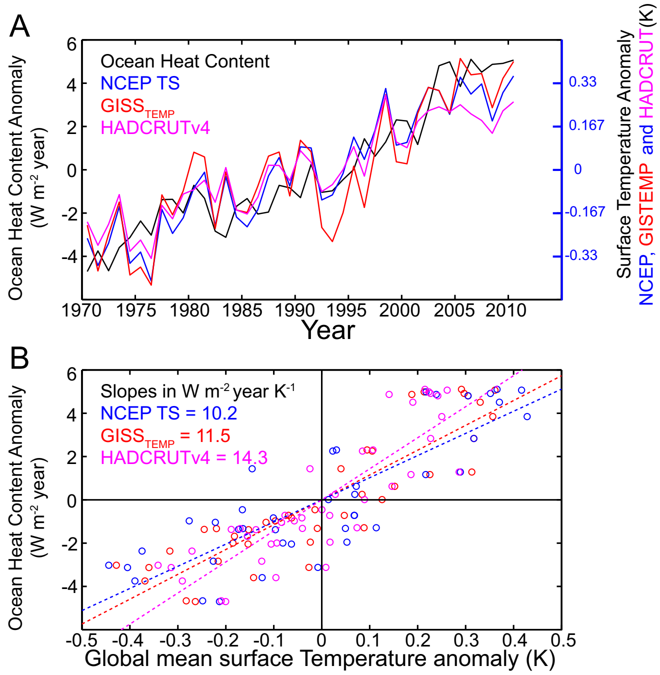

Fig. S2. (*A*) Time series of global ocean heat content anomaly (black line; left axis) and global mean surface temperature anomaly (TS, right axis) from NCEP reanalysis (NCEP TS; blue line), Goddard Institute for Space Studies Surface Temperature Analysis ($GISS_{TEMP}$ red line), and Office Hadley Centre surface temperature dataset verison 4 (HADCRUTv4; purple line) datasets. (*B*) Scatterplot of heat content and surface temperature anomaly. Each circle is an annual average anomaly, and the dashed line is the linear best fit that represents the climate system heat capacity (values given); 1 W m^{-2} y K^{-1} equals 7.6 m equivalent ocean depth.

Table S1. CMIP5 GCMs used in this study and the LW and SW feedbacks and forcings in the 4× CO_2 simulations

Model	λ_{SW}	λ_{LW}	F_{SW}	F_{LW}	τ_{cross}	SWEAR
CSIRO (Commonwealth Scientific and Industrial Research Organisation, Australia), and BOM (Bureau of Meteorology, Australia) ACCESS 1.0	0.8	−1.5	−0.6	6.3	32	1.0
Beijing Climate Center, China Meteorological Administration BCC CSM1.1	0.5	−1.7	0.4	6.3	22	1.2
Canadian Centre for Climate Modelling and Analysis CCCma canESM2	0.4	−1.4	1.5	6.1	16	1.4
National Center for Atmospheric Research NCAR CCSM4	0.6	−1.9	0.5	6.8	19	1.2
Centre National de Recherches Meteorologiques CNRM CM5	0.5	−1.6	2.1	5.1	7	1.8
Commonwealth Scientific and Industrial Research Organisation in collaboration with the Queensland Climate Change Centre of Excellence CSIRO MK3.6	1.3	−1.9	−1.3	6.3	16	1.2
LASG, Institute of Atmospheric Physics, Chinese Academy of Sciences LASG-IAP FGOALS	0.5	−1.3	−0.9	8.4	149	0.6
National Oceanic and Atmospheric Administration Geophysical Fluid Dynamics Laboratory GFDL CM3	1.2	−2.0	0.0	5.8	12	1.4
National Oceanic and Atmospheric Administration Geophysical Fluid Dynamics Laboratory GFDL ESM2MG	−0.1	−1.4	0.9	5.7	157	0.2
National Oceanic and Atmospheric Administration Geophysical Fluid Dynamics Laboratory GFDL ESM2M	0.1	−1.4	0.3	6.1	158	0.1
National Aeronautics and Space Administration Goddard Institute for Space Studies NASA-GISS E2 R	−0.3	−1.3	0.3	6.9	231	0.0
Institute for Numerical Mathematics INM CM4	0.5	−2.0	−0.8	7.0	166	0.2
Institut Pierre-Simon Laplace IPSL CM5A	1.2	−1.9	2.9	3.4	2	3.0
Institut Pierre-Simon Laplace IPSL CM5B	0.9	−1.9	1.2	4.0	6	2.0
Atmosphere and Ocean Research Institute (The University of Tokyo), National Institute for Environmental Studies, and Japan Agency for Marine-Earth Science and Technology MIROC 5	0.3	−1.9	2.0	6.5	13	1.0
Max Planck Institute for Meteorology MPI ESM	1.5	−1.6	1.9	6.4	11	1.4
Meteorological Research Institute MRI CGCM3	1.0	−2.2	0.1	6.4	11	1.6
Norwegian Climate Centre NCC NorESM1	0.7	−1.8	0.3	5.8	29	0.9
ENSEMBLE MEAN	0.6	−1.7	0.6	6.1	19	1.1
Observations	0.8 ± 0.4	−2.0 ± 0.3				

Also shown is the SWEAR over the 140-y 1% CO_2 simulations. The units are as follows: λ_{SW} and λ_{LW} (watts $meter^{-2}$ $Kelvin^{-1}$), F_{SW} and F_{LW} (watts $meter^{-2}$), and τ_{cross} (years).

Table S2. Estimates of radiative feedbacks using interannual regressions between forcings adjusted the Clouds and the Earth's Radiant Energy System Energy Balanced and Filled Product radiation data and various surface temperature datasets

Temperature data	λ_{SW}	λ_{LW}	λ
NCEP reanalysis TS	0.7 ± 0.4	−1.7 ± 0.2	−1.0 ± 0.3
GISTEMP	0.8 ± 0.4	−2.2 ± 0.3	−1.4 ± 0.4
Hadley Centre surface temperature dataset verison 4–CW HadCRUT4	0.9 ± 0.5	−2.0 ± 0.4	−1.1 ± 0.4
Average	0.8 ± 0.4	−2.0 ± 0.3	−1.2 ± 0.4

All values are in watts meter^{-2} Kelvin^{-1}. Uncertainties are assessed as 1 SD of the regression coefficient uncertainty.